Quantitative Mapping of the Orientation of Fibroin β-Sheets in *B. mori* Cocoon Fibers by Scanning Transmission X-ray Microscopy

Daniel Hernández Cruz,[†] Marie-Eve Rousseau,[‡] Marcia M. West,[†] Michel Pézolet,[‡] and Adam P. Hitchcock*,[†]

Department of Chemistry and BIMR, McMaster University, Hamilton, Ontario, Canada L8S 4M1, and Département de Chimie et CERSIM, Université Laval, Québec, Québec, Canada G1K 7P4

Received December 12, 2005; Revised Manuscript Received January 20, 2006

The spatial distribution of the linear dichroic signal associated with aligned β-sheets in a microtomed section of a *Bombyx mori* cocoon silk fiber was derived from scanning transmission X-ray microscopy (STXM). The intense C 1s → π^*_{amide} peak at 288.25 eV was found to have negligible dichroic signal in transverse sections but a large dichroic signal in longitudinal sections. This is consistent with other measurements of the orientation of the aligned β-sheets in silk fibers, in particular with those obtained by polarized Raman microspectroscopy to which our results are compared. When the dichroic signal strength is mapped at better than 100 nm spatial resolution, microscopic variations are found. Although the magnitude of the dichroic signal changes over a fine spatial scale, the direction of the maximum signal at any position does not change. We interpret the spatial variation of the intensity of the dichroic signal as a map of the quality of local orientation of the β-sheets in the fiber. At sufficiently high magnification and resolution, this technique should image individual β-sheet crystallites, although the present implementation does not achieve that. A map of the orientation parameter $\langle P_2 \rangle$ is derived. The average value of $\langle P_2 \rangle$ (-0.20 ± 0.04) from STXM is smaller than that derived from the analysis of the amide I band in polarized Raman spectra (-0.41 ± 0.03). This deviation is attributed to the fact that the STXM results also include the signal from unaligned regions of the protein.

Introduction

Molecular orientation strongly affects the physical properties of synthetic and natural macromolecular systems. Orientation is introduced in commercial polymers during processing as it is introduced naturally in biopolymers during their synthesis. For synthetic polymers, it has been shown that the deformation of thermoplastics induces the alignment of the molecular chains which results in an increase of the material strength.[1,2] Some level of control over chain orientation can be achieved in synthetic materials, but current processes generally allow only control of the primary and secondary structures in homopolymers and copolymers. On the contrary, living organisms are able to synthesize biopolymers (such as proteins) of high molecular weight with structural organization controlled at all levels. Actin, keratin, collagen, and silk[3] are a few examples of fibrous proteins characterized by hierarchical molecular order. Their biosynthesis is based on self-assembly and implies the total control of the primary sequence, the secondary structure, and the three-dimensional chain organization. The precision by which living systems achieve such a remarkable control over chain organization accounts for the high diversity of function (mechanical support, connective tissues, etc.) and mechanical properties of biopolymers.

The ultimate target of most studies of protein fibers is to characterize their structural organization in order to gain insights on how to improve synthetic fibrous polymers. The repetitive nature of fibrous proteins is reminiscent of synthetic polymers. In fact, most fibrous proteins are characterized by short amino acid repetitive motifs that often adopt a specific conformation crucial to the structural organization. In the case of the silks produced by silkworms and spiders, these repetitive motifs are rich in glycine, alanine, and serine which mainly adopt a β-sheet conformation.[4] For example, the primary amino acid sequence of the fibroin core of the cocoon silk produced by the domesticated silkworm *Bombyx mori* (*B. mori*) is dominated by the periodic $[Gly\text{-}Ala\text{-}Gly\text{-}Ala\text{-}Gly\text{-}Ser]_n$ hexapeptide sequence.[5] It is now well accepted that this particular sequence adopts the antiparallel β-sheet conformation and has the capability to form nanosized crystals.[6]

The more recent structural models developed to understand the mechanical properties of silk all agree that the β-sheet regions play a major role in establishing the high tenacity of silk fibers.[7−10] The combination of strength and toughness of native silks could be explained in part by the dispersion of small crystallites, mainly composed of β-sheets, in an amorphous-like matrix.[7] In the past, several techniques have been used to characterize the β-sheet orientation in silk fibers such as X-ray diffraction,[11−14] NMR spectroscopy,[9] birefringence,[15] and recently Raman microspectroscopy.[16] Each technique has its strengths and limitations. X-ray diffraction gives quantitative information about the ordering in both crystalline and amorphous regions of the material but can only provide that information at a spatial resolution dictated by the spot size, which is typically mm (lab based) or at best 10's of microns (synchrotron). NMR spectroscopy is only sensitive to certain nuclei. Birefringence gives the overall chain orientation. Raman spectroscopy gives bands due to amide vibrations that are characteristic of the presence of β-sheets, but they overlap with bands associated with other conformations. On the other hand, these techniques

* To whom correspondence should be addressed. Telephone: (905) 525-9140, ext. 24749. Fax: (905) 521-2773. E-mail: aph@mcmaster.ca.
[†] McMaster University.
[‡] Université Laval.

10.1021/bm050943u CCC: $33.50
Published on Web 02/16/2006

are complementary and provide valuable information on the intra- and intermolecular alignment of the β-sheets. Nevertheless, recent results from our laboratory (unpublished data) have shown that the mechanical properties of the silk threads are not only associated with the orientation of the β-sheets in the silk proteins, which are mostly aligned parallel to the fiber axis, but that other parameters such as the β-sheet content and organization (microstructure) have to be taken into account. Recently, Drummy et al.[17] have used diffraction and imaging modalities in a low voltage electron microscope (LVEM) to study crystallites in fibroin fibers. The technique we employ in this work quantitatively measures the orientation parameter at high spatial resolution and has the potential to directly visualize β-sheet domains. It is complementary to the LVEM approach.

Near edge X-ray absorption fine structure spectroscopy (NEXAFS),[18] using linearly polarized synchrotron light, provides a quantitative measurement of the direction and magnitude of orientation in anisotropic systems. Linear dichroic X-ray absorption signals can also be recorded at high spatial resolution (<50 nm) using scanning transmission X-ray microscopy (STXM).[18,19] In the past, STXM has been used to measure spatial distributions of molecular orientation in Kevlar fibers,[20,21] in crystals of small molecules,[22] and in polymers aligned by tensile stress.[23] Our overall goal is to develop linear dichroism NEXAFS microscopy as a reliable tool for quantitative orientation mapping of natural and synthetic fibers. Here we present the first results from STXM measurements of *B. mori* silkworm cocoon fibers. This type of silk was selected since it is well characterized in the literature and has a relatively simple repetitive primary amino acid sequence. We describe the measurement technique and the procedures used to derive orientation maps from polarization dependent images. The quantitative results are then compared to those obtained by Raman microspectroscopy. Recently, industries have sought to biomimic the process of spider silk production and have successfully produced high molecular weight silk proteins in mammalian cells.[24] Although the monofilaments obtained have toughness and modulus values comparable to those of native spider dragline silk, they show significantly lower tenacity. We hope that structure−property relationships developed by combined STXM and Raman microspectroscopy will assist the efforts to produce fibers from man-made fibroin which have equivalent mechanical properties to the natural fibers.

Experimental Section

Materials and Sample Preparation. Cocoons from the silkworm *B. mori* were supplied by the Insects Production Unit of the Canadian Forest Service (Sault-Ste-Marie, Ontario, Canada). *B. mori* cocoons were emptied and several fibers were taken manually from the intermediate layers of the cocoons. When manipulating the fibers, extra care was taken to prevent excessive mechanical strain (below 2%) to preclude any changes to the native molecular orientation. For Raman measurements, the native (i.e., not degummed) silk samples were gently mounted on glass microscope slides with double-sided tape. Prior to embedding for microtomy, silk fibers were kept in a dry environment away from sunlight. Blocks for microtomy were prepared by carefully placing native fibers in an aliphatic amine epoxy optimized for STXM.[25] Approximately 100 nm thick sections were cut perpendicular to the fiber axis (transverse sections) and parallel to the fiber axis (longitudinal sections). The sections were placed on TEM grids for STXM analysis.

STXM. X-ray imaging and spectroscopy were carried out at the Advanced Light Source using an interferometrically controlled STXM microscope at beamline 5.3.2 (STXM 5.3.2).[26,27] Images, spectra, and image sequences in the C 1s region were recorded from both transverse and longitudinal sections. The polarization dependence was obtained by manually rotating the sample, which involved opening the microscope, removing the sample, physical rotation (facilitated by mounting the TEM grid on a small gear riveted onto the support plate), reinserting the sample, finding the same region, and recording the next set of images. The linear polarization fraction is assumed to be 85%, similar to other bend magnet beamlines.[28] After each measurement, an image at 288.25 eV was recorded over a larger area to monitor the extent of radiation damage. As discussed below, we found that orientational order is more sensitive to radiation damage than bond-breaking or mass loss.

The as-recorded transmission signals were converted to optical densities (absorbance) using incident flux (I_o) signals measured through an adjacent hole. The signal at 288.25 eV consists of a combination of the C 1s $\rightarrow \pi^*_{amide}$ peak and an underlying signal from other transitions associated with the protein backbone and side chains. To isolate the π^*_{amide} signal from the background, two different procedures were used. In the first procedure (upon which most of the data in this paper is based), the signal below and above the 288.25 eV peak in the spectrum was linearly interpolated to determine the optical density (OD) at 288.25 eV associated with the non-π^*_{amide} signal. This value was then subtracted from each pixel in the single-energy images recorded at 9 angles, such that the signal in the fiber region of the processed image is the π^*_{amide} signal. A second procedure, applied in later work, recorded three images at 287.4 eV, 288.25 eV, and 289.0 eV for each rotation angle. The C 1s $\rightarrow \pi^*_{amide}$ signal was then derived by subtracting a weighted sum of the 287.4 and 289 eV images from the 288.25 eV image: $I_{\pi^*} = I_{288.25} - {}^1/_2(I_{287.4} + I_{289.0})$. In addition to the correction for the non-π^* signal, small variations in the optical density in the region of the epoxy were found. Since the epoxy is totally amorphous, we have interpreted the variations in the epoxy signal as uncontrolled instrumental response variations, either in the image or the I_o measurement (the signal recorded without sample). This small remaining variation was applied as a scaling factor to the π^*_{amide} images in order to remove the variations in the epoxy signal. This scale factor ranged from 0.97 to 1.03. After this step, the quality of the angular dependent signals was improved considerably.

Each corrected π^*_{amide} image was then rotated and aligned with the other images. These aligned, angle-dependent images were then combined into a 'polarization image sequence' which was subjected to a singular value decomposition (SVD) analysis[29−31] using a constant and the function $\cos^2\theta$ as the reference signals, where $(\theta - 90)$ is the angle between the long axis of the fiber and the E vector. The image and spectral processing was carried out using aXis2000.[32]

Raman Microspectroscopy. The polarized Raman spectra were recorded under controlled conditions of temperature (20.0 ± 0.5 °C) and relative humidity (35 ± 5% RH) in the backscattering configuration using a LabRam 800HR Raman spectrometer (Horiba Jobin Yvon, Villeneuve d'Ascq, France) coupled to a Olympus BX 30 fixed stage microscope. The 514.5 nm line of an argon ion laser (Coherent, 70C Series Ion Laser, Santa Clara, CA) was focused with a 100× objective (0.9 NA-Olympus) to a diameter of approximately 1 μm, generating an intensity of 5 mW at the sample. The confocal hole and the entrance slit of the monochromator were fixed at 200 and 100 μm, respectively. By using a 600 lines/mm holographic grating, it was possible to acquire a spectral window of 1650 cm^{-1} in one exposure on a one-inch open electrode Peltier-cooled CCD detector (1024 × 256 pixels) (Andor Technologies, Belfast, Northern Ireland). Polarized spectra (I_{XX}, I_{XZ}, I_{ZZ}, and I_{ZX}; where Z is the fiber axis and X is the transverse direction) were acquired for 30 s on three points on three different native fibers. The order parameter $\langle P_2 \rangle$ was calculated for each point, as described elsewhere.[16] The standard deviation determined takes into account the error of the measurements as well as the natural variability of silk fibers.

Results and Discussion

Imaging and Spectroscopy. Figure 1a presents the C 1s absorbance spectra of the three chemical components of the

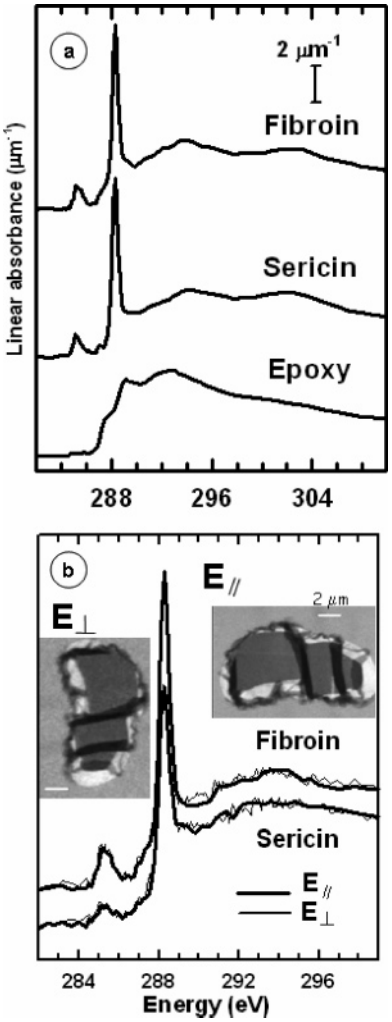

Figure 1. (a) C 1s NEXAFS spectra of the fibroin core, the sericin sheath and the embedding epoxy from a transverse cross section (with *E* vector perpendicular to the fiber axis). (b) C 1s NEXAFS spectra of the fibroin and sericin regions in the two orthogonal orientations shown in the absorbance images at 288.25 eV (*E* vector parallel and perpendicular to the long axis of the fiber transverse section).

system: the fibroin core, the sericin sheath, and the embedding epoxy. These spectra were recorded from a transverse section with the *E* vector parallel to the wider dimension of the transverse section (see inset images in Figure 1b). The spectra have been converted to absolute linear absorbance by matching the signal below 284 eV and above 310 eV to that predicted by the elemental composition (derived from the known amino acid sequence[5]) and a density of 1.3 g·cm^{-3}.[33] Table 1 lists the energies and proposed assignments of the spectral features. The C 1s spectrum of proteins is dominated by the intense C 1s → π^*_{amide} transition at 288.25 eV.[34,35] The small peak at 285 eV arises from C 1s → π^*_{ring} transitions of aromatic side chains. The broad peaks at 294 and 302 eV correspond to overlapping C 1s → σ^* transitions, with the 294 eV peak correlated to longer single C−O or C−C bonds and the 302 eV peak associated with shorter C═O double bonds. The spectrum of the aliphatic amine epoxy[25] has relatively little low lying structure, with a shoulder at 287.6 eV and a weak peak at 289.3 eV being assigned to C−H resonances, whereas the main broad peak at 292.4 eV is attributed to overlapping C 1s → σ^*_{C-C}, σ^*_{C-N}, σ^*_{C-O} transitions. Figure 1b compares the fibroin and sericin spectra recorded with the sample in two orthogonal orientations

Table 1. Peak Positions and Proposed Assignments of C 1s Spectral Features of Fibroin, Sericin, and Epoxy Resin[a]

energy (eV)					
fibroin		sericin		amine epoxy	assignment
XC	LO	XC	LO		
285.2	285.2	285.2	285.2		$\pi^*_{C=C-ring}$
287.1	287.2 (sh)	287.2 (sh)	287.2 (sh)		C−H
				287.5 (sh)	C−H
288.25	288.25	288.25	288.25		π^*_{amide}
				289.3	C−H
291.2 (w)	291.2 (w)	291.2 (w)	291.3 (w)		
				292.7	σ^*_{C-C}, σ^*_{C-N}, σ^*_{C-O}
293.9 (6)	293.6 (6)	293.9 (6)	293.6 (6)		$\sigma^*_{single\ bonds}$
				301.6	σ^*
302.4 (8)	301.4 (8)	302.4 (8)	301.7 (8)		$\sigma^*_{double\ bonds}$

[a] Abbreviations: XC = transverse section, LO = longitudinal section, sh = shoulder, w = weak; standard deviation is indicated between parentheses.

relative to the *E* vector (parallel and perpendicular to the wider dimension of the fiber transverse section). The spectrum of each component is the same in both sample orientations within the statistical precision. This indicates that the carbonyls are uniaxially distributed around the fiber axis. This is consistent with the structural picture from X-ray crystallography.[11−14]

Raman imaging of transverse sections (unpublished results) shows that the sericin sheath is much more porous, thus less dense, so that the epoxy can partly penetrate this layer. The spectrum of sericin displayed in Figure 1 has had a ∼30% contribution of epoxy signal subtracted from the spectrum extracted from the sericin region. After this processing, the C 1s spectra of sericin and fibroin are found to be very similar to those of other proteins.[30,34,35] Even though the spectra are quite similar, there are small differences in the fine details between the low lying π^* peaks at 285.2 and 288.25 eV and in the dip after the main π^* peak. When these spectra are used as reference signals for an SVD analysis of the C 1s image sequence of the transverse section, there is a clean and accurate separation of the components, as illustrated in Figure 2 which presents the epoxy, fibroin, and sericin component maps, and a color composite. These maps were derived by fitting a C 1s image sequence (83 images between 282 and 320 eV) to the 3 spectra shown in Figure 1a. Clearly, the fibroin and sericin components are identified in the fit, even in the right part of the imaged region, where the sericin sheath overlaps the fibroin core. That structure was probably formed during the sample preparation as the overlying strand also contains epoxy, suggesting that a mixture of epoxy and sericin from the right-hand upper side of the section was dragged across the fibroin core during microtoming. This example suggests that, at least in favorable cases, it is possible to use minor differences in the NEXAFS spectra of specific proteins to differentiate and thus map them in mixed systems. To our knowledge, this is the first time NEXAFS has been shown to be able to differentiate two proteins.

Figure 3 shows the C 1s NEXAFS spectrum of the fibroin core of a longitudinal section recorded with the *E* vector parallel and perpendicular to the fiber axis (to within 5°) (see the inset images of the two orientations). The spectrum of sericin in the longitudinal section (not shown) was the same as that for sericin in the transverse section and the same for the two orientations of the fiber relative to the *E* vector. A dramatic change was found in the fibroin spectrum, in that the 288.25 eV π^*_{amide} transition is much more intense when the fiber axis is perpendicular to the *E* vector relative to the case when it is parallel. Since the spectra in Figure 3 (as with those in Figure 1) have

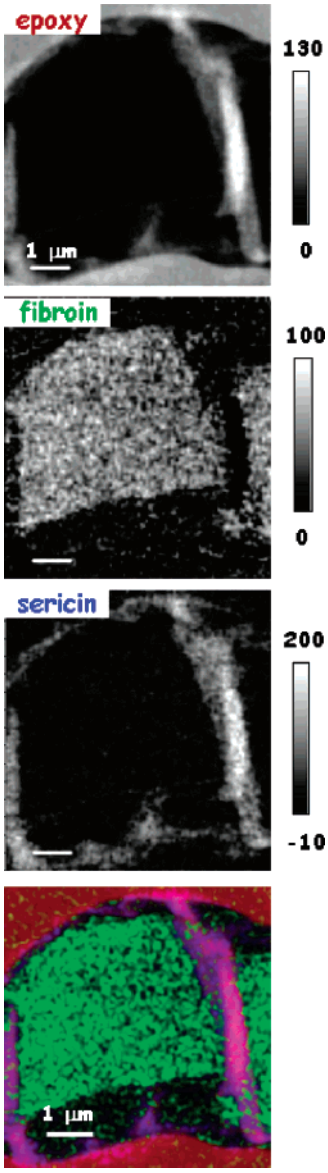

Figure 2. Component maps of the epoxy, fibroin, and sericin of the transverse cross-section derived by singular value decomposition of a C 1s image sequence with 83 energies (282−306 eV) to the C 1s spectra in Figure 1a. A color coded composite map (red = epoxy, green = fibroin, blue = sericin) is shown at the bottom. The gray scale indicates thickness in nm.

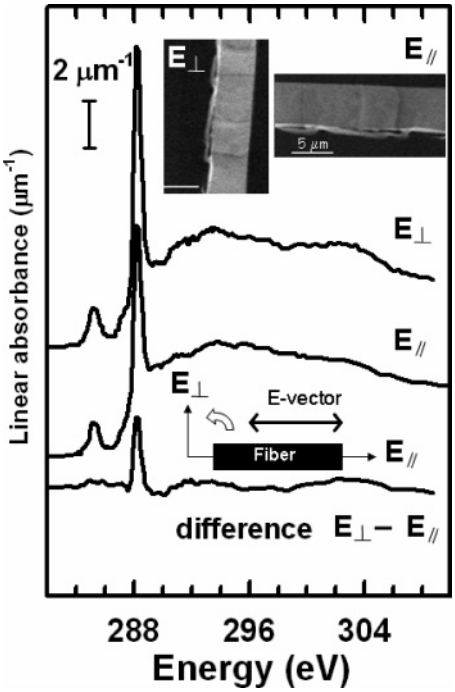

Figure 3. C 1s NEXAFS spectra of the fibroin core in a longitudinal cross-section, measured with the *E* vector approximately parallel and perpendicular to the fiber axis, along with the difference spectra. Inset images for both orientations illustrate the contrast difference at 288.25 eV. The sketch indicates the coordinate system used.

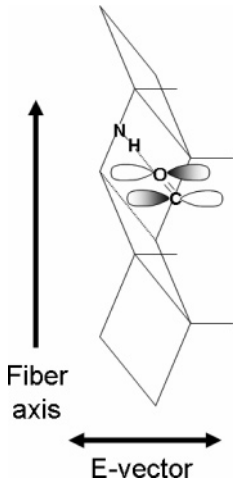

Figure 4. Schematic representation of the structure of the antiparallel β-sheets in fibroin.

been placed on a linear absorbance scale, the change in the 288.25 eV signal must be interpreted as an effect of linear dichroism.[28,36] The fact that the larger intensity occurs when the fiber axis is perpendicular to the *E* vector indicates that the π^* orbitals of some peptide C═O groups are preferentially oriented perpendicular to the fiber axis. These oriented $\pi^*_{C=O}$ orbitals are most likely located in the β-sheet regions that are known to be preferentially aligned along the fiber axis.[7,9−16] A schematic representation of the β-sheet structure in the silk fiber is presented in Figure 4 illustrating how the carbonyl orbitals must be aligned in order to explain the sign of the dichroic signal.

Quantitative Determination of the Orientation. As noted above, the 288.25 eV X-ray absorption band is due to excitation of an electron from the C 1s(C═O) orbital to the $\pi^*_{C=O}$ unoccupied energy level. The transition moment vector (*M*) for this absorption band is thus perpendicular to the plane of the peptide bond. Since STXM is an optical transmission technique, the absorbance (*A*) or OD of the 1s → $\pi^*_{C=O}$ transition should vary with the cosine square of the angle γ between the electric vector *E* of the incident radiation and the transition moment vector *M*. Thus, the intensity should be maximum when *E* is parallel to *M* and zero when *E* and *M* are perpendicular. On the basis of this polarization dependence, it is possible to quantify the level of orientation of the carbonyl groups from the dichroic ratio (*R*) measured experimentally[36]

$$R = \frac{A_{\parallel}}{A_{\perp}} \tag{1}$$

where $A_{\parallel}$ and $A_{\perp}$ are the absorbance of the band at 288.25 eV when the *E* vector of the X-ray beam is polarized parallel and perpendicular to the fiber axis. Since dichroism was not observed in the transverse sections, we can infer that the carbonyls are

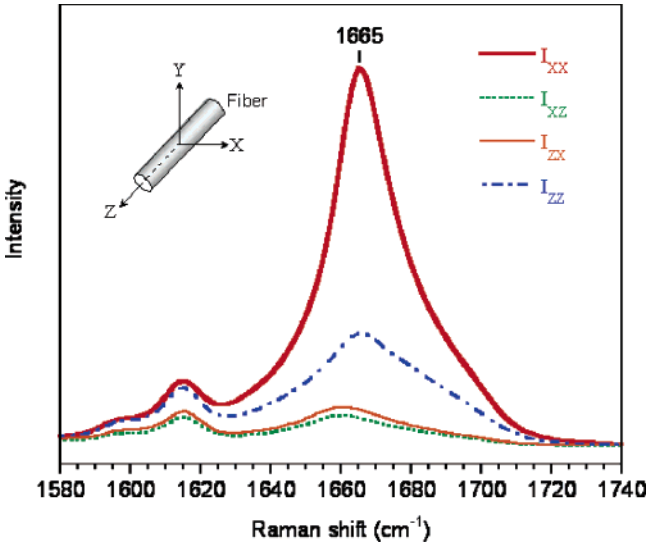

Figure 5. Polarized Raman spectra of native *B. mori* cocoon silk in the amide I region.

isotropically distributed around the fiber axis. For such a system with uniaxial symmetry around the fiber axis, the dichroic ratio can be used to calculate the second moment of the orientation distribution expressed as a sum of Legendre polynomials in cos γ[37]

$$\langle P_2(\cos\gamma)\rangle = \frac{3\langle\cos^2\gamma - 1\rangle}{2} = \frac{R-1}{R+2} \qquad (2)$$

The parameter $\langle P_2(\cos\gamma)\rangle$ or $\langle P_2\rangle$ is often called the order parameter or orientation function. It gives an average value of the distribution of orientation of the structural units inside the sample with respect to the reference axis. In a macromolecular system such as silk proteins, the notion of order parameter is especially important since the structural units in reality have a distribution of orientation instead of a definite orientation such as in a crystal. For an isotropic sample, $\langle P_2\rangle = 0$. For an oriented sample, $\langle P_2\rangle = 1$ if all of the transition moments are perfectly oriented parallel to the fiber axis, whereas $\langle P_2\rangle$ is -0.5 and 0 for perfect orientation at 90° and 54.7°, respectively. As described below, the average value of the orientation parameter derived from STXM is $\langle P_2\rangle = -0.20 \pm 0.04$. The negative $\langle P_2\rangle$ value obtained for *B. mori* fibroin in raw silk samples indicates that the carbonyl groups are predominantly oriented perpendicular to the fiber axis. This is in good agreement with the structural model of the oriented β-sheets found in fibroin,[7,9−16] as illustrated in Figure 4.

For comparison, the orientation of the proteins in raw silk fibers was also studied by polarized Raman microspectroscopy. An average value of $\langle P_2\rangle$ of -0.41 ± 0.01 was determined over 9 measurements (from 3 different points on 3 different samples) using the peak height of the band at 1665 cm^{-1} that is due to the β-sheet structure and following a procedure described elsewhere.[16] The averaged polarized spectra obtained in the amide I region (associated with the carbonyl stretching vibration of the amide groups) for native silk samples are shown in Figure 5. Surprisingly, the value of $\langle P_2\rangle$ determined for native silk (-0.41 ± 0.01) is somewhat higher and more reproducible (smaller standard deviation between 9 series of polarized spectra) than the results reported previously for degummed fibers (-0.36 ± 0.03).[16] This result suggests that the degumming process in hot water changes the level of orientation of the molecular chains to some extent. This observation is in agreement with the lower mechanical properties observed for degummed silk fibers compared to native silks.[38]

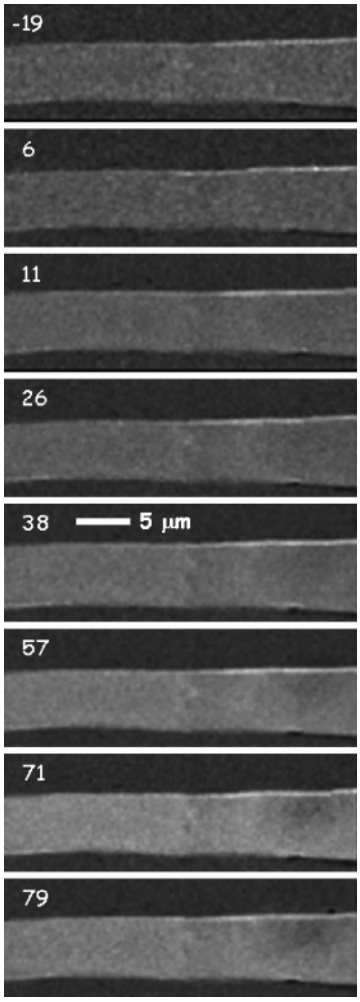

Figure 6. Aligned absorbance images at 288.25 eV of a longitudinal cut of a *B. mori* fiber at 8 different angles between the fiber axis and the *E* vector. These images were modified to correct for the non-π^* signal, equalized for the epoxy signal, rotated, and aligned as described in the text. Note that the radiation damage in area B (see Figure 7) is most apparent in the right side of the last of these images recorded at 79°.

The results for characterizing the orientation of silk fibroin in raw *B. mori* fibers by STXM and Raman microspectroscopy are in good qualitative agreement. They both indicate that the carbonyl groups are preferentially oriented perpendicular to the fiber axis. However, the value of $\langle P_2\rangle$ obtained by STXM (-0.20 ± 0.04) is lower than that obtained by Raman (-0.41 ± 0.01). This difference is most likely due to the fact that the Raman amide I band of silk fibers is dominated by the contribution of the carbonyls incorporated in the β-sheet structures, as shown in Figure 5, whereas the STXM technique is sensitive to all of the carbonyl groups within the sample, regardless of the secondary structure in which they are involved. It is also possible that the use of microtoming techniques, necessary to obtain a sample thin enough for transmission measurements by STXM, might lower the level of orientation of the proteins in the fibers.

Mapping of the Orientation of the β-Sheets. Figure 6 shows images at 288.25 eV of a longitudinal section recorded at 8 angles relative to the *E* vector. These images are all plotted on the same optical density scale. Relative to the original OD images, they were corrected by subtraction of underlying non-π^* signal, normalized to give identical signal in the epoxy

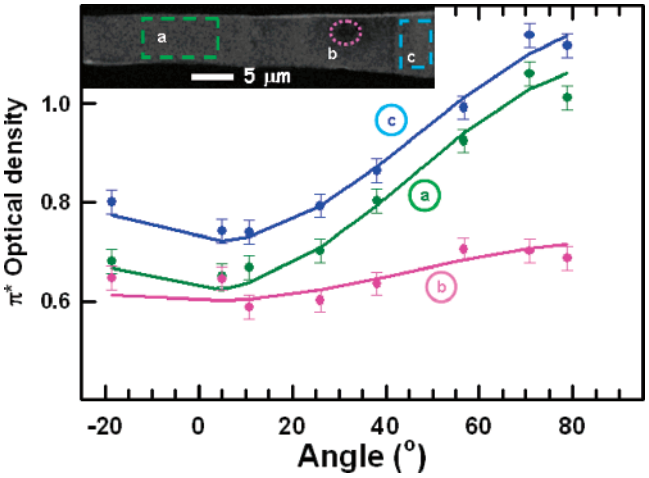

Figure 7. Fits of the angular variation of the π^*_{amide} signal extracted from three regions of the angle-scan sequence. The three regions are indicated in the top image, which is that of the 71° orientation. A spreadsheet was used to optimize the fit by systematically adjusting three parameters: the relative contributions of a constant (representing un-oriented regions), $\cos^2(\theta - \theta_o)$, and the angle of maximum intensity (θ_o).

Table 2. Average Orientation Parameters for Selected Regions of a Longitudinal Section of a *B. mori* Fiber, Derived from Angle Variation of the π^*_{amide} Intensity[a]

	analyzed regions		
parameters	A (left)	B (damaged)	C (right)
θ_o[b]	87(3)	86(4)	88(3)
polarized	0.90(6)	0.31(4)	0.85(7)
unpolarized	1.7(1)	1.7(1)	1.9(1)
% − pol	35(3)	15(3)	31(3)
$\langle P_2 \rangle$	−0.20(4)	−0.04(3)	−0.19(4)

[a] Letters A, B, and C refer to regions shown in Figure 7. All parameters were identified using a trial-and-error approach with a spread sheet. The uncertainties are based on the change needed to see deviations from visual best fit. [b] θ_o refers to the angle of maximum signal intensity.

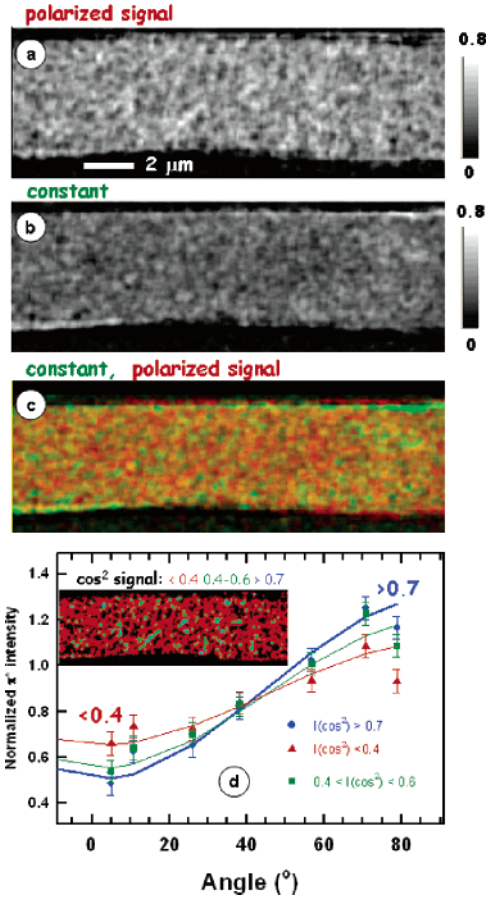

Figure 8. Spatial distribution of the magnitude of β-sheet orientation, derived by fits to the angle-dependent sequence. (a) Map of $\cos^2\theta$ component. (b) Map of a constant (un-oriented component). (c) Color coded composite (red = polarized signal in $\cos^2\theta$, green = constant, with each component scaled to fill the full color range). (d) Extracted angular signals from low, medium and high pixels of the orientation map (inset to d) color coded map of the pixels from which the angular signals were extracted.

region, and then rotated and aligned so that they have the same spatial scale and pixel spacing. One sees a systematic increase in the intensity of the fiber with increasing θ, with the maximum intensity when the fiber axis is close to perpendicular to the E vector.

These images were assembled into a single angle-dependent image sequence to facilitate quantitative analysis. Figure 7 shows the results of curve fits to the angle-dependent signals extracted from three regions, indicated as A, B, and C. Two of these regions, labeled A and C, were areas where only the image at 288.25 eV was recorded (Figure 6), whereas in region B, a full image sequence was also recorded at each angle. Quantitative results for the oriented fraction and the unoriented fraction in these regions, along with error estimates, are listed in Table 2. Area B received a relatively high radiation dose (~3 MGy) because many images were recorded at each fiber orientation. The area was clearly damaged by the end of the series of image sequences (see the bottom two images in Figure 6). The dose used was significantly lower than the characteristic dose derived for chemical damage as seen for other proteins (~100 MGy, as indicated by the loss of the $\pi^*_{C=O}$ intensity and increase of a new peak at 286.7 eV).[39] The spectrum of area B in the final image sequence was similar to that of other proteins. However, the angular dependence in this area was greatly reduced relative to the lower-dose regions (A and C). This strongly suggests that when proteins are X-irradiated the molecular orientation, in this case the alignment of the β-sheets and adjacent protein chains, or the microstructure that might confine the aligned chains, is modified at lower doses than those needed for other chemical changes, such as carbonyl bond breaking or mass loss.[39]

As discussed above, for a system with fiber symmetry such as silk, the β-sheet orientation can be described by the fit coefficients for the $\cos^2\theta$ signal and presented as a spatial map of the orientation magnitude. Inspections of many different regions showed that indeed, the angular dependence of the signal is such that maximum signal occurs when the fiber is oriented perpendicular to the E vector, indicating that the oriented domains are the same throughout the fiber. Figure 8 shows an orientation map of this region of the longitudinal section of *B. mori* fiber, derived by fitting the angle-dependent, corrected images to $cos^2\theta$ and a constant. The mottling in the map of the $\cos^2\theta$ signal is much greater than that in the constant. To verify that the variation in the "orientation magnitude map" is real, pixels with various magnitudes were identified by masking techniques and the extracted signals are displayed in Figure 8d, along with fits to $\cos^2\theta$ and a constant. Clearly, as one selects pixels with a greater intensity in the $\cos^2\theta$ component map, the angular variation of the intensity is considerably greater, verifying the analysis and the existence of small (few hundred nm) domains which are more oriented than adjacent regions. We interpret these more highly oriented regions as related to

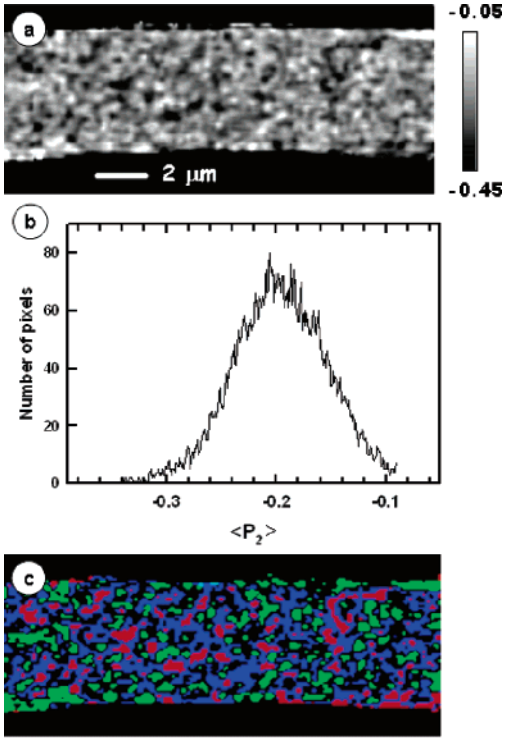

Figure 9. Spatial distribution of the values of the orientation parameter, derived as described in the text. (a) Map of $\langle P_2 \rangle$ component. (b) Histogram of $\langle P_2 \rangle$ values. (c) Color coded map of $\langle P_2 \rangle$ values. Red indicates $\langle P_2 \rangle < -0.25$, blue $-0.25 < \langle P_2 \rangle < -0.2$, black $-0.20 < \langle P_2 \rangle < -0.15$, and green, $\langle P_2 \rangle > -0.15$.

uneven spatial distributions of the β-sheet crystallites. At lower spatial resolution, these results are consistent with the results of Drummy et al.[17] In that low voltage electron microscopy study of microtomed longitudinal sections of *B. mori* silk fibers, the images showed seemingly random arrangements of 5−10 nm crystallites. Selected area diffraction confirmed there was no patterning in the ordering which is consistent with the absence of an apparent ordering in the orientation magnitude map shown in Figure 8. When the image of Drummy et al.[17] is smoothed to approximate the STXM resolution, the contrast is much reduced, but there is still a mottling similar to that seen in the STXM results. Thus we believe the orientational mapping by STXM is detecting "clumps" from uneven spatial distributions of the crystallites. Another aspect of β crystallites in *B. mori* is observations of significant anisotropy in the shapes of single crystallites.[12,13,17] However, this effect is significantly beyond the spatial resolution of current STXM technology to detect.

To convert the STXM measurements to a map of the $\langle P_2 \rangle$ orientation parameter, the images measured at angles of 5° and 79° between the *E*-vector and the fiber axis were processed with the framework described in eqs 1 and 2. Corrections were applied for the small difference from the 0° and 90° values, as well as for the incomplete linear polarization of the radiation. Together these corrections resulted in reducing the magnitude of the 5° $\pi^*_{C=O}$ map by 7% and increasing the magnitude of the 79° $\pi^*_{C=O}$ map by 8%. The resulting map of the $\langle P_2 \rangle$ values is presented in Figure 9a. Although the magnitudes are changed by the transformation from the $\cos^2 \theta$ component map to the $\langle P_2 \rangle$ map, the spatial distributions are very similar, except that the sense of the gray scale is reversed: black areas in the $\langle P_2 \rangle$ map correspond to more oriented regions, whereas white areas in the polarized component map correspond to more oriented regions. To explore the spatial distribution of the $\langle P_2 \rangle$ values in greater detail, the histogram of $\langle P_2 \rangle$ values over the area displayed was calculated (Figure 9b). As can be seen, this histogram displays a Gaussian shape and is centered at a $\langle P_2 \rangle$ value of −0.20. This result is in agreement with the shape of the most probable distribution of orientation calculated from the $\langle P_2 \rangle$ and $\langle P_4 \rangle$ values obtained for the amide C═O groups by Raman microspectroscopy.[16] The $\langle P_2 \rangle$ histogram was also used to create Figure 9c, which is a color coded locator map of pixels with values of $\langle P_2 \rangle$ in specific ranges (red has $\langle P_2 \rangle < -0.25$, blue corresponds to $\langle P_2 \rangle$ values between −0.25 and −0.20, black has $\langle P_2 \rangle$ between −0.20 and −0.15, and green has $\langle P_2 \rangle > -0.15$). Thus, the red regions are more oriented, and the green regions are less oriented. Although this helps to visualize the spatial distribution of the orientation, at least at this level of spatial resolution (where the smallest "isolated" regions of high orientation are of the order of 100 nm), there is no apparent regular pattern. Three possible reasons could be postulated: (1) no such pattern exists; (2) there is a pattern, but it can only be discerned at much higher spatial resolution; (3) there is a pattern at some spatial scale, but it requires three-dimensional order mapping to visualize. In the case of *B. mori*, the results of Drummy et al.[17] strongly suggest that there is no patterning, at least in a 2D presentation.

In summary, we have presented for the first time a microscopic method that allows quantitative mapping of orientation in a representative protein sample with a spatial resolution better than 100 nm. The methodology can be applied readily to other natural and synthetic fibers, such as spider silk. It could be useful to investigate the homogeneity of fibers as well as the presence of an orientation-based skin−core structure. Although the individual images are similar in character to those for Kevlar presented by Ade et al.,[20,21] this work extends the method to the generation of quantitative orientation maps of either the polarized component or derived $\langle P_2 \rangle$ values. At present, the process of manually rotating samples is rather time-consuming and, even if it was motorized, would still be relatively slow due to the need to relocate the rotated fiber and reset the field of view. However, the same results can be achieved with a stationary sample and field of view, if one uses an elliptically polarized undulator to rotate the electric vector.[40] A STXM is mounted on an EPU-equipped beam line at the ALS (beamline 11.0.2) and a similar system is being implemented and will soon be available at the Canadian Light Source.[41]

Acknowledgment. This research was supported by Natural Science and Engineering Research Council (NSERC, Canada), Canada Foundation for Innovation, and the Canada Research Chair programs. We thank Dr. Gary Mitchell for providing the rotational sample plate used in the STXM 5.3.2. measurements. Construction and operation of the STXM 5.3.2 microscope is supported by NSF DMR-9975694, DOE DE-FG02-98ER45737, Dow Chemical, NSERC, and the Canada Foundation for Innovation. We thank David Kilcoyne and Tolek Tyliszczak for their contributions to developing and maintaining the instrument. The Advanced Light Source is supported by the Director, Office of Energy Research, Office of Basic Energy Sciences, Materials Sciences Division of the U.S. Department of Energy, under Contract No. DE-AC03-76SF00098.

References and Notes

(1) Ward, I. M. *Structure and Properties of Oriented Polymers*, 2nd ed.; Chapman & Hall: London, 1997; pp 1−41.
(2) White, J. L.; Cakmak, M. In *Encyclopedia of Polymer Science and Engineering*; Mark, H., Bikales, N., Overberger, C., Menges, G., Eds.; John Wiley & Sons: New York, 1987; Vol. 10, pp 595−636.
(3) Renuart, E.; Viney, C. In *Structural Biological Materials, Design and Structure−Property Relationships*; Pergamon Material Series; Elices, M., Ed.; Pergamon: Oxford, 2000; Chapter 8, pp 221−267.

(4) Gosline, J. M.; Demont, M. E.; Denny, M. W. *Endeavour* **1986**, *10*, 37−43.
(5) Zhou, C. Z.; Confalonieri, F.; Medina, N.; Zivanovic, Y.; Esnault, C.; Yang, T.; Jacquet, M.; Janin, J.; Duguet, M.; Perasso, R.; Li, Z. G. *Nucleic Acids Res.* **2000**, *28*, 2413−2419.
(6) Lotz, B.; Colonna-Cesari, F. *Biochimie* **1979**, *61*, 205−214.
(7) Termonia, Y. *Macromolecules* **1994**, *27*, 7378−7381.
(8) Termonia, Y. In *Structural Biological Materials*; Pergamon Material Series; Pergamon: New York, 2000; Vol. 4, pp 337−349.
(9) Simmons, A. H.; Michal, C. A.; Jelinski, L. W. *Science* **1996**, *271*, 84−87.
(10) van Beek, J. D.; Hess, S.; Vollrath, F.; Meier, B. H. *Proc. Natl. Acad. Sci. U.S.A.* **2002**, *99*, 10266−10271.
(11) Work, R. W.; Morosoff, N. *Text. Res. J.* **1982**, *52*, 349−356.
(12) Grubb, D. T.; Ji, G. *Int. J. Biol. Macromol.* **1999**, *24*, 203−210.
(13) Grubb, D. T.; Jelinski, L. W. *Macromolecules* **1997**, *30*, 2860−2867.
(14) Riekel, C.; Müller, M. *Macromolecules* **1999**, *32*, 4464−4466.
(15) Carmichael, S.; Barghout, J. Y. J.; Viney, C. *Int. J. Biol. Macromol.* **1999**, *24*, 219−226.
(16) Rousseau, M.-E.; Lefevre, T.; Beaulieu, L.; Asakura, T.; Pezolet, M. *Biomacromolecules* **2004**, *5*, 2247−2257.
(17) Drummy, L. F.; Phillips, D. M.; Koerner, H.; Vaia, R. A.; Farmer, B. L.; Naik, R. R. *Microsc. Microanal.* (Suppl. 2) **2005**, *11*, 1268−1269.
(18) Ade, H. In *X-ray Spectromicroscopy, Experimental Methods in the Physical Sciences*; Samson, J. A. R., Ederer, D. L., Eds.; Academic Press: New York, 1998; Vol. 32, pp 225−249.
(19) Ade, H.; Urquhart, S. G. *Chemical Applications of Synchrotron Radiation*; Sham, T. K., Ed.; World Scientific Publishing: Singapore, 2002; pp 285−355.
(20) Smith, A. P.; Ade, H. *Appl. Phys. Lett.* **1996**, *69*, 3833−3835.
(21) Ade, H.; Hsiao, B. *Science* **1993**, *262*, 1427−1429.
(22) Croll, L. M.; Britten, J. F.; Morin, C.; Hitchcock, A. P.; Stover, H. D. H. *J. Synchrotron Radiat.* **2003**, *10*, 265−268.
(23) Koprinarov, I.; Demirors, M.; Tylisczak, T.; Kilcoyne, A. L. D.; Hitchcock, A. P.; Ade, H.; Mitchell, G. E. *2001 ALS Compendium Abstr.* **2002**, 163−164.
(24) Lazaris, A.; Arcidiacono, S.; Huang, Y.; Zhou, J.-F.; Duguay, F.; Chretien, N.; Welsh, E. A.; Soares, J. W.; Karatzas, C. N. *Science* **2002**, *295*, 472−476.
(25) Zheng, G.; Croll, L. M.; West, M.; Araki, T.; Stöver, H. D. H.; Hitchcock, A. P. **2005**, manuscript in preparation.
(26) Kilcoyne, A. L. D.; Tyliszczak, T.; Steele, W. F.; Fakra, S.; Hitchcock, P.; Franck, K.; Anderson, E.; Harteneck, B.; Rightor, E. G.; Mitchell, G. E.; Hitchcock, A. P.; Yang, L.; Warwick, T.; Ade, H. *J. Synchrotron Radiat.* **2003**, *10*, 125−136.
(27) Warwick, T.; Ade, H.; Kilcoyne, A. L. D.; Kritscher, M.; Tylisczcak, T.; Fakra, S.; Hitchcock, A. P.; Hitchcock, P.; Padmore, H. A. *J. Synchrotron Radiat.* **2002**, *9*, 254−257.
(28) Stöhr, J. In *NEXAFS Spectroscopy*; Springer Tracts in Surface Sciences; Springer: Berlin, 1992; Vol. 25.
(29) Koprinarov, I. N.; Hitchcock, A. P.; McCrory, C.; Childs, R. F. *J. Phys. Chem. B* **2002**, *106*, 5358−5364.
(30) Hitchcock, A. P.; Morin, C.; Zhang, X.; Araki, T.; Dynes, J. J.; Stover, H.; Brash, J. L.; Lawrence, J. R.; Leppard, G. G. *J. Electron Spectrosc.* **2005**, *144−147*, 259−269.
(31) Zhang, X.; Balhorn, R.; Mazrimas, J.; Kirz, J. *J. Struct. Biol.* **1996**, *116*, 335−344.
(32) aXis2000 is written in Interactive Data Language (IDL). It is available free for noncommercial use from http://unicorn.mcmaster.ca/aXis2000.html.
(33) Vincent, J. F. V. In *Structural Materials*; Macmillan: London, 1982; pp 1−378.
(34) Loo, B. W.; Sauerwald, I. M.; Hitchcock, A. P.; Rothman, S. S. *J. Microsc.* **2001**, *204*, 69−86.
(35) Lawrence, J. R.; Swerhone, G. D. W.; Leppard, G. G.; Araki, T.; Zhang, X.; West, M. M.; Hitchcock, A. P. *Appl. Environ. Microbiol.* **2003**, *69*, 5543−5554.
(36) Buffeteau, T.; Pézolet, M. Linear Dichroism in Infrared Spectroscopy. In *Handbook of Vibrational Spectroscopy*; Chalmers, J. M., Griffith, P. R., Eds.; John Wiley and Sons: West Sussex, U.K., 2002; Vol. 1, pp 693−710.
(37) Stein, R. S. *J. Polym. Sci.* **1958**, *31*, 327−334.
(38) Perez-Rigueiro, J.; Elices, M.; Llorca, J.; Viney, C. *J. Appl. Polym. Sci.* **2002**, *84*, 1431−1437.
(39) Morin, C.; Hitchcock, A. P.; Li, L.; Zhang, X.; Araki, T.; Doran, A.; Scholl, A. *J. Electron Spectrosc.* **2005**, in preparation.
(40) Young, A. T.; Arenholz, E.; Marks, S.; Schlueter, R.; Steier, C.; Padmore, H. A.; Hitchcock, A. P.; Castner, D. G. *J. Synchrotron Radiat.* **2002**, *9*, 270−274.
(41) Kaznacheyev, K.; Blomqvist, I.; Hallin, E.; Urquhart, S. G.; Loken, D.; Tylisczak, T.; Warwick, T.; Hitchcock, A. P. In *Principles of Optical Design of the SM Beamline at the CLS*, Synchrotron Radiation Instrumentation 2003: Eighth International Conference on Synchrotron Radiation Instrumentation; Warwick, T., Arthur, J., Padmore, H. A., Stöhr, J., Eds.; American Institute of Physics: Melville, 2004; Vol. 705, pp 1303−1307.

BM050943U